Article

Integrated pH Sensors Based on RuO$_2$/GO Nanocomposites Fabricated Using the Aerosol Jet Printing Method

Mahtab Taheri, Mohsen Ketabi, Ahmad M. Al Shboul, Shirin Mahinnezhad, Ricardo Izquierdo, and M. Jamal Deen*

Read Online

ACCESS | Metrics & More | Article Recommendations

ABSTRACT: An aerosol jet printing (AJP) process for depositing ruthenium dioxide (RuO$_2$) as a promising material for pH sensing is reported. Graphene oxide (GO) with a large surface area was used for the in situ sol−gel deposition of RuO$_2$ nanoparticles on its surface. The cosolvent ratio and solid loading of the solution are adjusted to form a printable and stable ink. The monodispersed aerosol was atomized on the surface of the screen-printed carbon electrode in order to develop an integrated pH sensor. The RuO$_2$−GO pH sensor demonstrates excellent performance, with a rapid response time of less than 5 s and high sensitivity in the pH range of 4−10. Compared to traditional carbon electrodes, the RuO$_2$−GO sensor shows up to four times higher sensitivity. The increased sensitivity is a result of the consistent attachment of small-crystallized RuO$_2$ nanoparticles onto the surface of GO sheets, leading to a synergistic effect. Thanks to the AJP method as a facile and cost-effective integration technique, the fabricated electrodes can serve as an alternative to traditional rigid pH electrodes for accurate pH measurement.
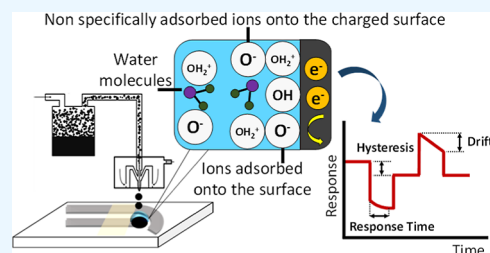
INTRODUCTION

Printing techniques are a widely explored method for the precise patterning of advanced nanomaterials and are used in various applications, including flexible displays, electronics packaging, and health-related sensors.[1−3] Among the established printing methods, aerosol jet printing (AJP), a 2D printing method, is a relatively recent addition to the printing toolbox. Its noncontact nature allows for precise, high-resolution structures, reaching as fine as 10 μm.[4,5] The noncontact feature minimizes contamination and material damage, ensuring sensor integrity. AJP's high-resolution capability enables precise deposition of functional materials, allowing for complex sensor architectures. Additionally, AJP is versatile and can handle various materials such as metal nanoparticles, metal oxides, semiconducting polymers, and carbon-based nanomaterials.[6−8] This versatility enables the customization of the sensors for specific applications. AJP is also scalable and suitable for both small-scale research and large-scale production, ensuring cost-effectiveness. However, the AJP of ruthenium oxide (RuO$_2$), a key material for electrochemical applications, is less commonly reported.

RuO$_2$ has gained considerable attention for numerous electrochemical applications due to its capability of driving reversible multielectron transfer redox reactions,[9−11] high electrocatalytic activity,[12] and affinity for hydrogen.[13] RuO$_2$-based materials have been used as electrode materials for supercapacitors,[14] active components for chlorine generation from HCl,[15] and as a catalyst for different reductions.[16,17]

Exploiting the intrinsic properties of RuO$_2$, we might consider some other potential applications in Li-ion batteries,[18] aerobic oxidation of alcohols,[19] and sensing materials in chemical sensors.[20−23] Previously, we demonstrated that the reversible redox reactions between RuO$_2$ and hydronium ions (H$_3$O$^+$) could be used for highly sensitive pH monitoring,[13] as pH is at the center of a wide range of health monitoring fields, including pharmaceuticals, food processing, environmental science, and biomedical applications.[24,25]

One important challenge in using RuO$_2$-based materials in low-cost electrochemical systems is its cost and deposition techniques, which hinder its frequent application despite its advantages, such as superb sensitivity, selectivity, rapid response, and stability under various environmental conditions.[26] Usually, RuO$_2$-based materials are fabricated using electrochemical deposition,[27] hydrothermal growth,[28] and expensive methods like sputtering.[29,30] A large amount of chemicals, high temperature, and high-pressure chambers (vacuum equipment) are some of the requirements of these processing techniques. Therefore, the use of these processing methods, along with the high cost of material, results in costly
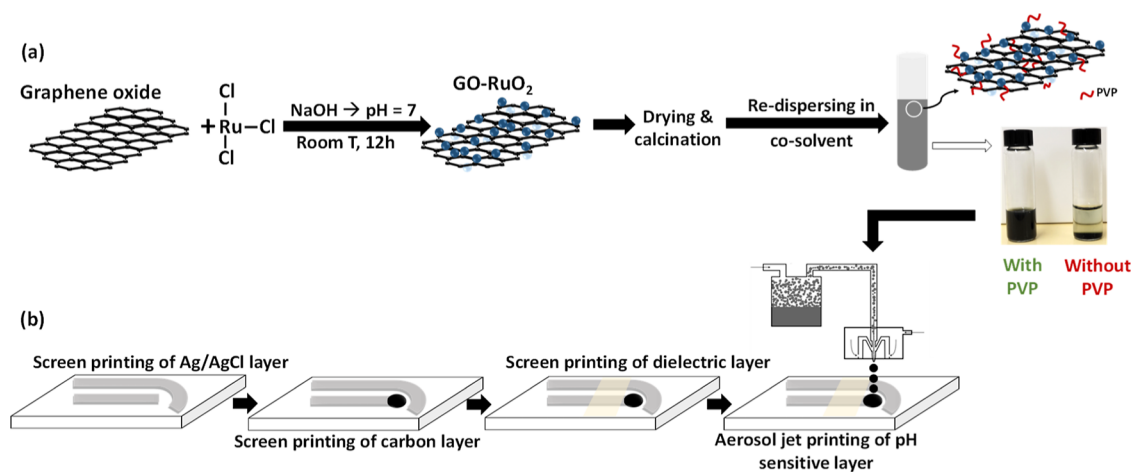
Figure 1. Schematic illustration of the (a) Process for preparing the nanocomposite of RuO_2-GO. (b) Screen printing processes of different layers of the pH sensor and the AJP process for the deposition of RuO_2/GO as the pH-sensitive material.

manufacturing, which may be unsuitable for the mass production of cost-efficient sensors.[31]

Hence, we suggest two approaches to reduce the expenses related to RuO_2 electrodes. First, we can blend RuO_2 with other chemically stable substances such as graphene and its derivatives such as graphene oxide (GO). Studies have demonstrated that these combinations enhance flexibility and stability. Additionally, the presence of surface oxygen functionalities on graphene oxide nanosheets can act as anchoring sites for forming RuO_2 nanoparticles (NPs). These smaller NPs with a heightened specific surface area, evenly dispersed on the surface of GO sheets, would offer more metal oxide centers for sensing, leading to increased pH sensitivity.[32] Furthermore, the even distribution of RuO_2 nanoparticles facilitates effective paths for sensing and conduction through the binding of proton and hydroxide ions and electron transfer, respectively. The second solution is applying a less complicated and more cost-efficient AJP technique for developing RuO_2 sensors.

This paper outlines our simple method for creating nanocomposites of RuO_2 and GO by depositing RuO_2 nanoparticles onto GO nanosheets using an in situ sol–gel process, with a focus on pH sensing. Achieving desirable functional characteristics in the depositions is heavily dependent on formulating an appropriate ink. To address this, we formulated an ink suitable for AJP utilizing the RuO_2/GO composite. Optimizing this ink's AJP process, we could deposit continuous and uniform thin films with good adhesion to the underlying screen-printed carbon paste substrates. Solid-state reference electrodes, in addition to the sensing electrodes, are also screen-printed to form potentiometric sensors. While RuO_2 and GO have been employed individually in creating electrochemical pH sensors, the synergistic use of these materials and their application via AJP has not been explored, to our knowledge. These inexpensive pH sensors, completely produced through printing processes, possess the potential for integration into upcoming portable electrochemical setups, distinguishing them from traditional pH test papers. For applications requiring continuous monitoring, higher accuracy, and precise quantification of pH levels, the developed pH sensor emerges as the preferred choice.

■ MATERIALS AND METHODS

Chemicals and Reagents. Powders of graphene oxide (consisting of 15−20 sheets with 4−10% edge oxidation), ruthenium(III)chloride ($RuCl_3$, containing 45−55% Ru), polyvinylpyrrolidone (PVP, molecular weight: 30,000), and sodium hydroxide (NaOH, purity ≥98%) were obtained from Sigma-Aldrich for creating the RuO_2/GO nanocomposite. 2-(2-Ethoxyethoxy)ethanol (commercial name: carbitol, >98%, CAS#111-90-0) and ethyl acetate (99.9%, CAS#141-78-6) were used for the preparation of the AJP solution containing the nanocomposite of RuO_2/GO. The commercial carbon black ink, dielectric passivation paste, and Ag/AgCl paste for screen printing were acquired from Henkel, DuPont, and Sigma-Aldrich, respectively. All chemicals were of analytical grade and used without further purification.

Synthesis of the RuO_2/GO Nanocomposite. RuO_2/GO nanocomposite preparation has been described in our previous work.[13] Briefly, the in situ sol–gel method was used to obtain RuO_2 nanoparticles over the surface of GO nanosheets. Initially, a homogeneous solution was formed by adding GO with a concentration of 1 mg/mL to DI water and subjecting it to 10 min of sonication. Following that, 500 mg of ruthenium chloride hydrate was combined with 100 mL of GO solution. Subsequently, the solution's pH was adjusted to 7 by introducing 1 M NaOH solution and vigorously stirring the mixture for 12 h at room temperature. The resulting suspension underwent centrifugation and was rinsed four times with DI water to eliminate NaCl, as indicated by the reaction:[33] $Cl_3 + 3NaOH \rightarrow 3Ru(OH)_3 + 3NaCl$. The resulting nanopowder was then dried at 100 °C for 2 h. Finally, a calcination step at 350 °C in the presence of air for 2 h was carried out to induce crystallization of the RuO_2 nanoparticles within the composite.

Since AJP would be utilized to fabricate pH-sensitive material (RuO_2/GO) over the surface of the carbon base layer, formulation of a suitable ink is key for deposition with desirable functional characteristics. For this purpose, PVP was added to the mixture of carbitol/ethyl acetate (2:10 v/v), followed by adding 120 mg of the synthesized nanocomposite and 60 mg of commercial carbon paste and ultrasonication for 2 h.

Screen Printing and AJP. Figure 1b illustrates the fabrication process of the four-layer pH sensor designed with
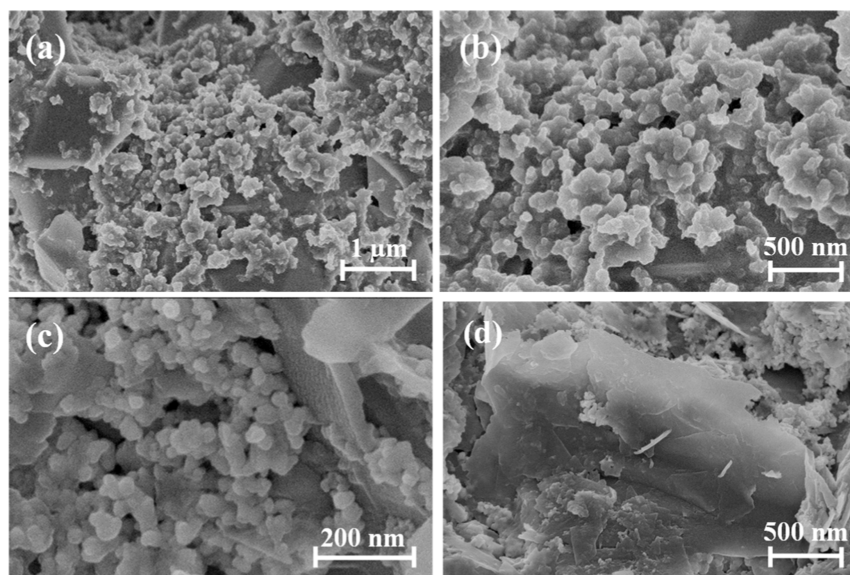
Figure 2. SEM images of (a−c) RuO$_2$-GO at different magnifications. (d) GO film.

two electrodes, a working electrode and a reference electrode. Commercial Ag/AgCl and carbon inks were printed on the PET surface via screen printing technology (Keko p200s) to create the reference and conductive layers, respectively. Then, a layer of commercial dielectric passivation layer was printed on the upper part of the working and reference electrodes, and then the electrode was dried in an oven at 120 °C. Next, to modify the surface of the active layer using RuO$_2$/GO, AJP (Optomec, Aerosol Jet, USA) with a 300 μm diameter nozzle and by fixing the carrier gas/sheath gas rates at 35 sccm/50 sccm was used. During AJP, the stage was maintained at 70 °C. The thin sensing films were printed on screen-printed carbon electrodes on a flexible PET substrate. Later, the printed sensors were incubated for 1 h at 120 °C in air.

Structural and pH Characterization. The structural and morphological analyses of the samples involved the use of an X-ray diffractometer (Bruker D8 DISCOVER diffractometer) with Cu Kα radiation (λ = 1.54184 Å, 40 kV, 40 mA) and an extreme high-resolution scanning electron microscope (FEI Magellan 400), respectively. The Renishaw InVia Laser Raman spectrometer was used to collect the Raman spectra. A 532 nm laser (1800 L/mm grating) with a power output of 50 mW was used to excite the samples.

For pH sensing, a PalmSens4 potentiostat was employed. The performance evaluation of RuO$_2$-based sensing electrodes followed a potentiometric setup against a printed reference electrode. The open-circuit potential between these electrodes was recorded at 1 s intervals for 20 s after immersing the electrodes in pH buffer solutions of pH 4, 7, and 10. The electrodes were transitioned between pH buffer solutions with cleaning using DI water. Additionally, the pH sensor's selectivity was assessed by introducing solutions with varying concentrations (10^{-6}, 10^{-4}, 10^{-3}, and 10^{-2} M) of potential interfering ions (CaCl$_2$, NH$_4$Cl, (NH$_4$)$_2$SO$_4$, Na$_2$SO$_4$, and KNO$_3$) into tap water. The pH of the tap water for each ion and specific concentration was measured using a commercial pH meter (Fisherbrand accumet AB150 pH Benchtop Meters).

RESULTS AND DISCUSSION

AJP Ink Formulation. Figure 1a illustrates the fabrication of a composite material, combining RuO$_2$ with GO, using the in situ sol−gel technique. When RuCl$_3$·xH$_2$O was introduced to GO, the solution's viscosity notably increased. This change can be attributed to the robust interaction between oxygen group anions (specifically hydroxyl, carboxyl, and epoxy groups) at the periphery and surface of graphene oxide and Ru^{3+} cations.[34] This interaction leads to the creation of active sites crucial for nucleation, growth, and anchoring of RuO$_2$ nanoparticles during the sol−gel process. Consequently, this process generates substantial cross-linking between GO sheets and ensures a uniform dispersion of nanoparticles on the graphene oxide surface.

After the RuO$_2$/GO nanocomposite was synthesized, the next step is formulating the ink suitable for AJP. Understanding the atomization technique and the rheological properties of the ink (viscosity, volatility, and density of the material) is needed to produce an aerosol with characteristics suitable for jetting. A monodispersed and highly dense aerosol with sufficient inertia is characteristic of an ideal aerosol. Aerosolization is achieved by applying either ultrasonic or pneumatic atomization.[35] This work used an ultrasonic atomizer to produce highly uniform aerosols. Therefore, material recommendations in terms of the predominant solvent type, maximum viscosity, and maximum solid loading should be considered during the formulation.

The first challenge is effectively controlling evaporation during atomization, transportation, and deposition. When only low-boiling-point solvents are used, the loss of mass due to their evaporation during transportation will lead to droplets with insufficient inertia for impaction. Therefore, the result would be the deposition of dry and discrete particles with high surface roughness features. To address this issue effectively, it is advisable to use a blend of solvents with varying levels of volatility. The higher-volatility solvent should evaporate soon after being atomized, saturating the carrier gas and maintaining a consistent droplet volume during transportation until the aerosol stream interacts with the sheath gas. Subsequently, the lower volatility solvent should start evaporating. To prevent

complete drying of the particles before deposition, it is recommended to incorporate 10% of a less volatile cosolvent in the ink.[36] Therefore, in this study, the mixture of carbitol and ethyl acetate with boiling points of 201 and 77 °C, respectively, were used as the cosolvent. This selection not only prevents the total drying of the particles before deposition but also enhances layer adhesion and allows higher functional material concentration, meeting equipment requirements. Moreover, the viscosity of the sensing ink is improved with the use of carbitol and ethyl acetate solvents, which is beneficial for aerosol jet printing. This combination helps to reduce the swelling of the printing plate's surface. The combination of carbitol and ethyl acetate solvents reduces the swelling of the printing plate's surface caused by ethyl acetate.

In our previous study, a functional material with a 0.5 mg/mL concentration was added to the solvent. However, according to the literature,[35] the viscosity and solid loading of dispersions for the ultrasonic atomization must be such that atomization can be conducted properly. Therefore, solid loading in the range of 20−55 wt % and solution viscosity in the 1−10 cP range are recommended.[35] Accordingly, the next challenge is controlling the monodisperse high-concentration particles within the solvent. Because dispersing the RuO_2/GO composite with a concentration of 10 mg/mL in the solvent is challenging, an additive, PVP, was employed. PVP is a large, safe,[37] and nonionic polymer[38] featuring a highly hydrophilic portion (the pyrrolidone segment) and a hydrophobic segment.[39] It can serve as a surface stabilizer and assist in dispersing $RuO2$ nanoparticles effectively in the medium. This is attributed to its functional groups, including CH_2, C−N, and C=O.[40] Thanks to the pyrrolidone ring's polar amide group and the nonpolar methylene and methine groups in both the ring and PVP's structure, the substance can dissolve well in water and various nonaqueous substances, such as alcohol-based and organic solvents.[41] Moreover, PVP acts as a stabilizer, inhibiting nanoparticle aggregation by generating repulsive forces through hydrophobic carbon chains that extend into the solvent and repel each other.

Morphological and Physical Characterization of the Nanocomposite. SEM was used to investigate the morphological aspects of RuO_2-GO and GO films (Figure 2). A three-dimensional porous structure of RuO_2 nanoparticles with varied sizes and shapes distributed densely and uniformly over the surface of interconnected GO nanosheets is shown in Figure 2a,b. This result is consistent with the explanation in the previous part, AJP ink formulation, showing the importance of GO sheets for the nucleation and growth of RuO_2 nanoparticles. In order to estimate the size of the RuO_2 NPs, higher SEM magnification was used. As shown in Figure 2c, the size of RuO_2 nanoparticles is in the range of 12−30 nm. Figure 2d shows GO sheets utilized in the synthesis of the RuO_2/GO composite without the presence of RuO_2 nanoparticles. It presents a morphology of irregular nanosheets forming aggregates due to van der Waals forces and $\pi-\pi$ interactions.

In order to confirm the homogeneous dispersion of anchored NPs across the interconnected GO sheets, energy-dispersive X-ray (EDX) analysis was used. In Figure 3a, the diagram illustrates the elemental patterns within the sample composite. Subsequently, Figure 3b−d depicts the outcomes of EDX analysis detailing the distribution of three elements: carbon, oxygen, and ruthenium. These findings closely align with the RuO_2-GO structure, affirming the uniform distribution of RuO_2 nanoparticles on the GO sheets. Additionally, the
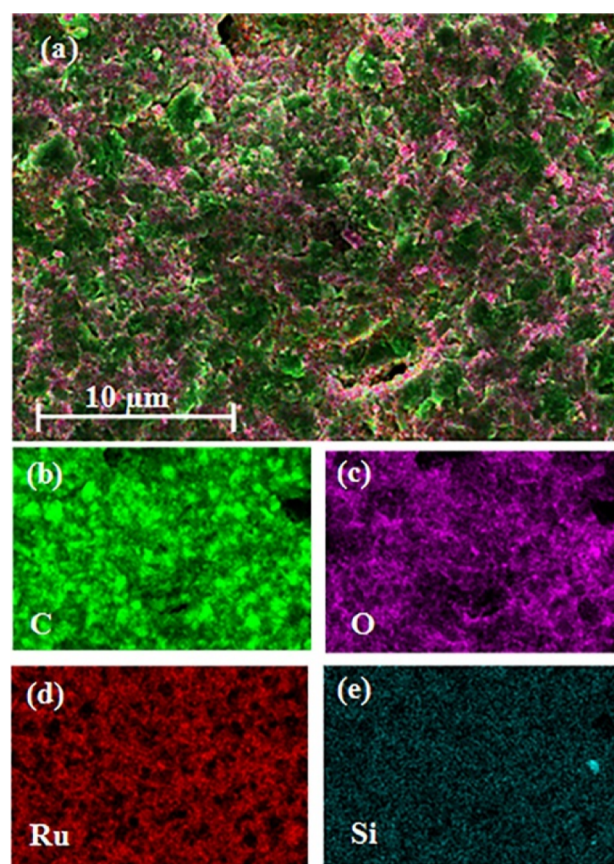

Figure 3. (a) SEM EDX mapping of the RuO_2−GO nanocomposite. SEM EDX analysis showing distribution of different elements: (b) Carbon (C). (c) Oxygen (O). (d) Ruthenium (Ru). (e) Silicon (Si).

appearance of Si in Figure 3e originates from the PET substrate.

As illustrated in Figure 4a, XRD analysis was carried out to validate the development of crystalline RuO_2 following the in situ sol−gel approach and subsequent calcination. The distinct and strong diffraction patterns confirm the presence of a well-defined crystalline structure in the form of rutile RuO_2 (JCPDS card number 65-2824). The highest intensity peak is noticeable at $2\theta = 35°$, signifying the tetragonal phase of RuO_2. Raman spectroscopy demonstrated the presence of the ruthenium oxide rutile crystal structure and graphene (in the form of GO or rGO) sheets in the composite, as seen in Figure 4b. The Raman spectrum of GO shows two key characteristic peaks: the D-band at 1337 cm^{-1}, which represents disordered sp^2 carbon atoms, and the G-band at 1569 cm^{-1}, which corresponds to the E_{2g} vibrational mode of sp^2 bonded carbon atoms.[42] GO typically contains oxygen-containing functional groups such as hydroxyl (−OH), epoxy (−O−), and carboxyl (−COOH) groups, leading to destruction of the graphene sp^2 structure.[43] In our work, GO before reaction with RuO_2 had a D/G ratio ∼0.86, indicating the partial oxidation of graphene flakes and maintaining a good graphene sp^2 structure. This suggests better electrical charge transfer throughout the graphene flakes. Upon reaction of GO with RuO_2, the D/G ratio decreased to ∼0.79, indicating the partial reduction of the GO to rGO after calcination. Another broad peak at 1082 cm^{-1} could be due to functional groups on the surface of the graphene oxide.[43] Furthermore, two peaks associated with ruthenium oxide are observed at 544 and 771 cm^{-1}, which
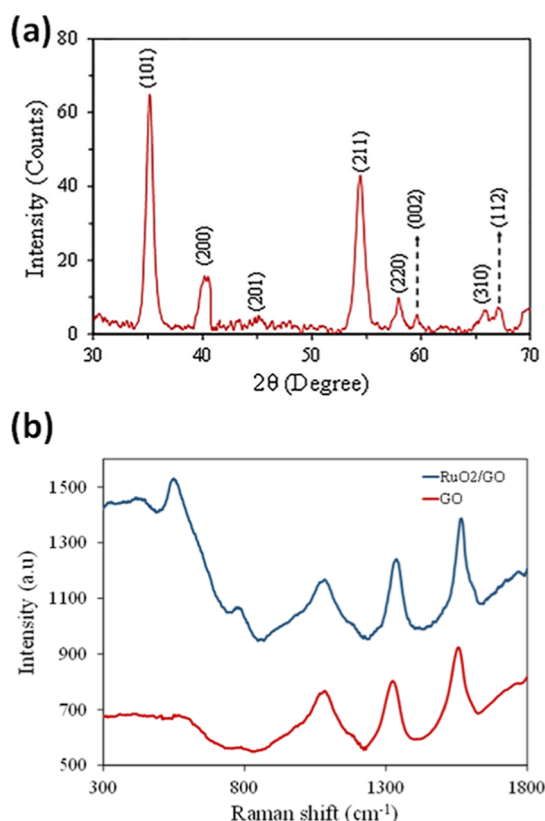
Figure 4. (a) XRD pattern of RuO_2. (b) Raman spectrum of GO and RuO_2/GO nanopowders.

correspond to major Raman-active modes of rutile RuO_2.[44] The Raman spectrum confirms integration between GO and RuO_2.

Electrochemical pH Measurement. *pH Sensing Performance.* The pH sensing performance was characterized by the open-circuit potentiometry (OCP) method, where an integrated electrode consisting of working and reference electrodes was used as a pH sensor. The performance of printed RuO_2/GO composite and pristine carbon paste for pH sensing was evaluated by immersing these two electrodes into buffer solutions in the pH range from 4 to 10 to cover a wide pH range. The pH-dependent output signals of both electrodes at room temperature are shown in Figure 5a. For the unmodified electrode, increasing the pH would result in a slight potential decrease, and during the measurement in a constant pH, a considerable change in the value of potential can be seen, which indicates its instability due to hydrogen trapping within carbon flakes. On the other hand, the existence of RuO_2 as the pH-sensitive material over the surface of the modified electrode would result in a larger change between 7 and 4 and 7 and 10. A greater electrode output potential corresponds to heightened sensitivity. As depicted in Figure 5b, the sensor we developed demonstrated a proportional and consistent response ($R^2 > 0.9898$) and nearly adhered to the Nernstian sensitivity (55.3 mV/pH), contrasting with the lower sensitivity of the original carbon electrode, which stands at 17 mV/pH. The significant boost in sensitivity of the modified sensor across a broad pH spectrum and its reliable performance over 5 cycles underscore the pivotal role of RuO_2 NPs in pH sensing. Consequently, this sensor proves valuable

for a diverse range of applications encompassing food, health, and environmental monitoring.[45]

In order to justify the role of RuO_2 NPs upon exposure to different pH buffer solutions, we need to discuss their pH sensing mechanism. When RuO_2 is in contact with an aqueous medium, sequential adsorption of water molecules occurs. During this process, hydrolysis occurs, involving the breaking of a metal−oxygen double bond to produce two hydroxide groups. This process follows one of the equilibrium equations.[46,47] Figure 5c shows the charged surface groups at the RuO_2−solution interface.

$$Ru^{(IV)}O_2 + e^- + H^+ \leftrightarrow Ru^{(III)}O(OH) \tag{1a}$$

$$RuO_2 + H_2O \leftrightarrow RuO(OH)_2 \tag{1b}$$
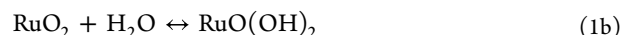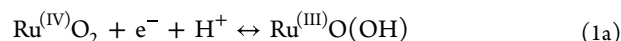
The presence of water molecules at the solid−liquid interface leads to amphoteric hydroxide layer formation through adsorption and dissociation. This layer can manifest as either $-OH_2^+$ or $-O^-$ sites.[48] In acidic solutions where protons are prevalent, the surface of the sensing material would primarily feature $-OH_2^+$ sites due to the abundance of hydrogen ions. The excess hydrogen ions subsequently facilitate the oxidation of hydrogen

$$H_2 \leftrightarrow 2H^+ + 2e^- \tag{2}$$

However, within an alkaline solution, a decrease in the concentration of H^+ ions leads to the creation of $-O^-$ sites, subsequently resulting in the reduction of oxygen[49]

$$O_2 + 4e^- + 2H_2O \leftrightarrow 4OH^- \tag{3}$$
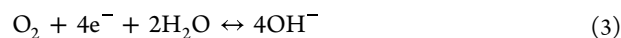
The levels of oxygen and hydrogen in water can be approximated by utilizing eq 4

$$H_2 + 2H_2O \leftrightarrow O_2 + 6H^+ + 6e^- \tag{4}$$
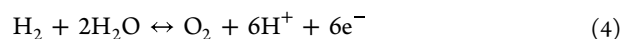
Using eqs 1a and 4, the Nernst response of RuO_2 would be

$$= E° + \frac{RT}{nF}\ln\left(\frac{\alpha[Ru^{III}]}{\alpha[Ru^{IV}] \cdot \alpha[H^+]}\right) + \frac{RT}{nF}\ln\left(\frac{p(O_2)}{p(H_2)}\right) \tag{5}$$

where E represents the voltage difference between the working and reference electrodes (mV), $E°$ stands for the standard redox potential (mV), R denotes the universal gas constant (8.314 J K^{-1} mol^{-1}), T signifies the temperature (K), n represents the charge of species, and F is the Faraday constant (96,485 C mol^{-1}). $\alpha[Ru^{III}]$, $\alpha[Ru^{IV}]$, and $\alpha[H^+]$ stand for respective ion activities, while $p(O_2)$ and $p(H_2)$ are the oxygen and hydrogen gas pressures, respectively. If we assume similar activities of Ru^{III} and Ru^{IV} (which approach 1 in the solid state), 1 electron transfer according to eq 1a, and considering pH $= -\log_{10} \alpha[H^+]$, the potential of a RuO_2-based electrode at room temperature is

$$= E° - 59.14\,\mathrm{pH} + \frac{RT}{nF}\ln\left(\frac{p(O_2)}{p(H_2)}\right) \tag{6}$$

Then, if we consider eq 4, for the 6-electron reaction, the final equation at room temperature becomes

$$= E° - 59.14\,\mathrm{pH} + 9.8\log\left(\frac{p(O_2)}{p(H_2)}\right) \tag{7}$$

Usually, when discussing the pH sensitivity of RuO_2, authors commonly omit the consideration of oxygen and hydrogen
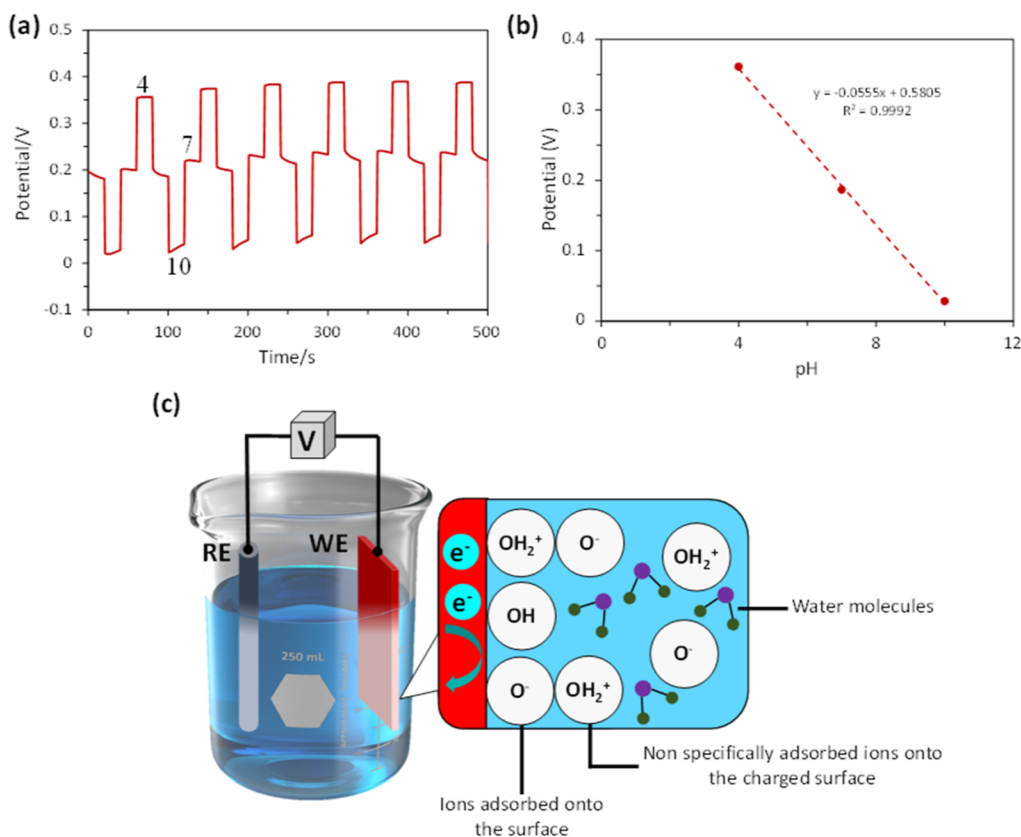
Figure 5. (a) Conducting OCP on screen-printed carbon electrodes, either unmodified or modified, by cycling the pH in the sequence 7−4−7−10 five times. (b) Sensitivity measurement of the modified sensor. (c) Adsorption of potential-determining ions on the surface of RuO_2 as the working electrode.

gases in the Nernst equation. This omission stems from the assumption that the concentrations of these gases remain constant within the medium.[50] Therefore, we would end up with the below equation

$$= E^\circ - 59.14 \, pH \tag{8}$$

Hysteresis. The accuracy of the sensor was determined by its hysteresis. Considering the results shown in Figure 5a, cycling the pH level from 7 to 10−7−4−7 would result in the hysteresis of 12 mV for the integrated sensor. This value is equivalent to a pH change of 0.22. Compared to the previous study[13] where drop casting was used for depositing the composite of RuO_2/GO over the surface of screen-printed carbon electrode, a higher hysteresis value could be seen here. This could be attributed to using carbitol with a high boiling point (201 °C) as the cosolvent to control the evaporation during atomization, transportation, and deposition. The high boiling point of this solvent prevents its complete removal during incubation, leaving some residual effect that would negatively affect the accuracy. This phenomenon could result in the slow diffusion of H^+ between the inner and outer surface of the sensing material and slow adjustment in the hydration of the electrode surface.[51] Therefore, replacing carbitol with another low volatile organic solvent that is miscible with ethyl acetate but with a lower boiling point could lead to a smaller hysteresis value. Thus, the hysteresis value for the developed sensor could be due to the residual effect of carbitol, diffusion of hydrogen ions into the nanocomposite, and the trapping of H_2 at the grain boundaries and between the graphene oxide nanoplates.

Response Time. The graph in Figure 6a illustrates the potential−time relationship of the RuO_2−GO nanocomposite across different pH levels, with the aim of evaluating its response time. The graph shows that the sensor achieves 90% of its equilibrium value within a span of less than 5 s after altering the buffer solution, whether it is an acidic or basic solution. This rapid response is attributed to the swift uptake and binding of ions from the external active surface of RuO_2−GO to the inner active surface. The nanoscale and microscale surface structure of the RuO_2/GO composite facilitates this phenomenon by promoting the diffusion of liquid ions into the intergrain regions and pores.

Drift. The pH sensor's drift performance was analyzed by immersing the combined sensor in a pH 7 solution for a period of under 2 h, as illustrated in Figure 6b. By selecting the first hour of measurement inside the dashed line box, the drift of the sensor was calculated at around 36 mV/h (0.65 pH/h), which is relatively large compared to the previously developed sensor using the same sensitive material but with a drop-casting method. In order to further investigate the stability of the sensor, instead of the printed reference electrode, an external reference electrode (Ag/AgCl) along with the printed working electrode was immersed in pH 7 for 10 h. As shown in Figure 6c, the drift decreased considerably to the value of 0.288 mV/h, indicating the working electrode's high stability over time. Therefore, we can conclude that the absence of an electrolyte (KCl) for the ion exchange would cause the instability of the printed reference electrode potential. In order to solve the problem with the high drift effect in the case of integrated electrodes, there is a need to develop a solid-state
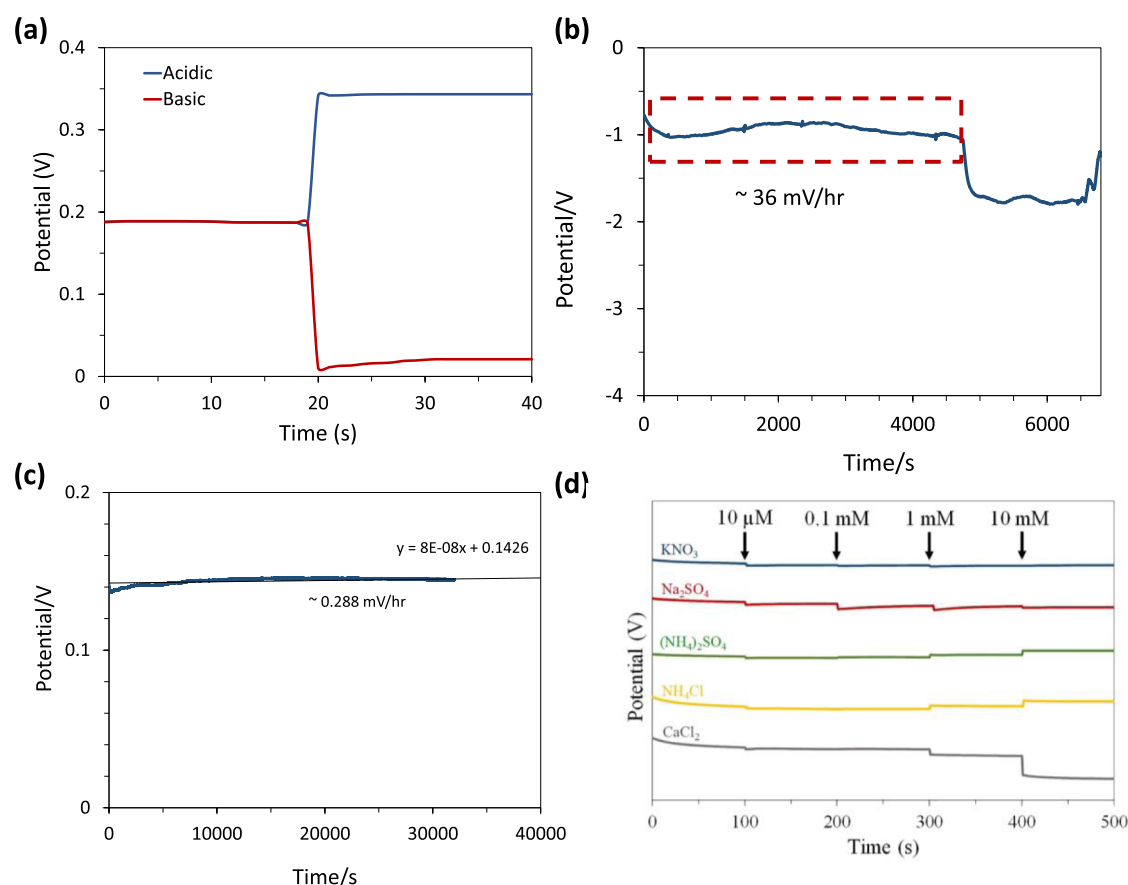
Figure 6. (a) Variation in response time for a sensor utilizing RuO_2-GO in diverse pH buffer solutions. (b) Fluctuation in pH sensor readings over a 10 h period at a pH level of 7. (c) pH sensor's temporal drift pattern over a 10 h period at pH 7, utilizing an external reference electrode. (d) Influence of pH sensor's response over time by the presence of seven commonly occurring interfering ions in water, with concentrations ranging from 10 μM to 10 mM.

reference electrode that is stable versus time and in different chemical environments.

Selectivity. The pH sensor's selectivity was assessed by introducing solutions containing different concentrations (ranging from 10 μM to 10 mM) of interfering ions like KNO_3, $Na_2(SO_4)$, $(NH_4)_2SO_4$, NH_4Cl, and $CaCl_2$, as illustrated in Figure 6d. The alterations in output potential for each concentration of the interfering ions were considered acceptable, taking into account the corresponding pH changes. The most noticeable shift in the pH response was observed when introducing 10 mM $CaCl_2$. This occurred due to the substantial $CaCl_2$ concentration, which reacts with the components in tap water to generate $Ca(OH)_2$, a potent base that significantly modifies the pH of the solution.

Figure 7 shows the stability of the integrated pH sensor when stored in air at room temperature for 14 days. It can be seen that the sensitivity of the sensor fluctuates slightly, indicating its high stability over time.

In Table 1, an overview of the pH sensing capabilities of oxides belonging to the Pt-group is presented. The last column of the table provides a straightforward calculation for a performance indicator known as the figure-of-merit (FoM)

$$FoM = \frac{\text{sensitivity}\left(\frac{mV}{pH}\right)}{\text{drift}\left(\frac{mV}{h}\right) \times \text{hysteresis (mV)} \times \text{response time (s)}} \quad (9)$$
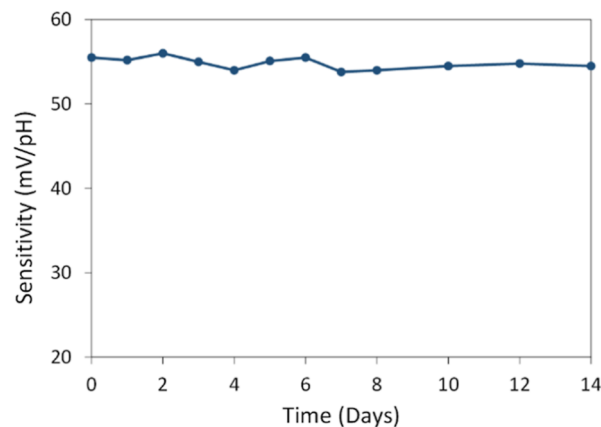

Figure 7. Lifetime measurement of the developed pH sensor.

The FoM is a measure of sensor performance, with higher values signifying greater sensitivity, reduced drift, decreased hysteresis, and faster response times. Our sensor, when using an external reference electrode, has the highest FoM value, which indicates its outstanding performance compared to other sensors. Our RuO_2/GO electrochemical pH sensor (last row in Table 1) is among the best of the Pt-group oxide (RuO_2, IrO_2, PdO) sensors ever reported. Considering the integrated sensor, it exhibited a relatively large drift effect (36 mV/h), which is due to the absence of ion exchange electrolytes over the surface of the printed reference electrode.

Table 1. Summary of the pH-Sensing Performances of Pt-Group Oxides Collected from the Literature

year, ref	material	deposition method	sensitivity (mV/pH)	drift (mV/h)	hysteresis (mV)	response time (s)	FoM
2023[52]	IrO$_2$	roll-to-roll	60.6	NG	9.5	NG	
2021,[53,54]	Pd/PdO	spin coating	57.5	0.52	9.8	20	0.56
2019[55]	RuO$_2$	sputtering	55.7	36	1.66	<30	0.03
2019[56]	RuO$_2$	electrodeposition	55	1	11	NG	
2019[56]	IrO$_2$	electrodeposition	72.2	0.083	3.61	NG	
2019[57]	Pt/IrO$_2$	electrodeposition	71.3	0.2		<6	
2018[58]	RuO$_2$	In situ sol−gel	58.1	0.8	NG	2	
2017[59]	RuO$_2$	sputtering	58.4	5	1.13	30	0.34
this work	**RuO$_2$/GO**	**AJP**	**55.5**	**36**[a]	**12**	**<5**	**0.026**[a]
				0.288[b]			3.21[b]

[a]Using an integrated pH sensor. [b]Using an external reference electrode.

This high value of drift would cause a considerable reduction in the FoM. Developing a solid-state reference electrode with higher potential stability over time would improve the performance characteristics of the sensor while using the AJP method as the facile and cost-effective integration technique. Another advantage of the developed sensors is that most other reported sensors require expensive and complex fabrication methods, making mass production difficult. However, our integrated RuO$_2$/GO sensor offers exceptional performance and the advantage of being produced at a low temperature using the AJP technique, which overcomes thermal limitations and enables low-cost mass production. With this method, the fabricated electrodes can be an alternative to both traditional rigid pH electrodes and a pH test paper for accurate measurement. This pH sensor offers real-time continuous monitoring, higher accuracy, and a wider pH range compared with traditional pH tests, making them ideal for dynamic processes and precise pH quantification.

CONCLUSIONS

We have developed an AJP process for developing an integrated pH sensor using the porous nanocomposite RuO$_2$/GO material. For the formulation of the suitable ink, the ratio of high/low volatility solvents and solid loading of the solution were adjusted to have stable and printable ink. Then, the monodispersed aerosol was atomized on the surface of the screen-printed carbon electrode, followed by annealing at the low temperature of 120 °C for 1 h to remove the solvents. The resulting RuO$_2$/GO electrode integrated with a solid-state reference electrode was used as the potentiometric sensor. The effective dispersion of RuO$_2$ nanoparticles, functioning as the sensing element, across the GO nanosheets facilitates rapid ion diffusion into the reactive inner surfaces, resulting in a quick response within 5 s. Moreover, the integrated sensor displayed consistent pH responses, exhibiting a sensitivity of 55.3 mV/pH. An evaluation of sensor precision and stability was carried out through hysteresis and drift assessments, yielding values of 12 and 36 mV/pH, respectively. The large drift effect is due to the absence of an ion exchange layer or electrolyte over the surface of the printed reference electrode, causing potential instability. By developing a solid-state Ag/AgCl electrode with higher potential stability, we would be able to build an electrochemical sensing platform with high sensitivity, fast response, stability, low cost, and ease-of-use for biomedical applications.

AUTHOR INFORMATION

Corresponding Author

M. Jamal Deen − *Electrical and Computer Engineering (ECE) Department, McMaster University, Hamilton, Ontario L8S4K1, Canada; School of Biomedical Engineering, McMaster University, Hamilton, Ontario L8S4K1, Canada;* orcid.org/0000-0002-6390-0933; Email: jamal@mcmaster.ca

Authors

Mahtab Taheri − *Electrical and Computer Engineering (ECE) Department, McMaster University, Hamilton, Ontario L8S4K1, Canada;* orcid.org/0000-0003-3702-3655

Mohsen Ketabi − *Department of Electrical Engineering, École de Technologie Supérieure, Montreal, Quebec H3C 1K3, Canada*

Ahmad M. Al Shboul − *Department of Electrical Engineering, École de Technologie Supérieure, Montreal, Quebec H3C 1K3, Canada;* orcid.org/0000-0002-7270-095X

Shirin Mahinnezhad − *Department of Electrical Engineering, École de Technologie Supérieure, Montreal, Quebec H3C 1K3, Canada*

Ricardo Izquierdo − *Department of Electrical Engineering, École de Technologie Supérieure, Montreal, Quebec H3C 1K3, Canada*

Complete contact information is available at:
https://pubs.acs.org/10.1021/acsomega.3c06309

Notes

The authors declare no competing financial interest.

REFERENCES

(1) Qin, Y.; Kwon, H. J.; Subrahmanyam, A.; Howlader, M. M. R.; Selvaganapathy, P. R.; Adronov, A.; Deen, M. J. Inkjet-Printed Bifunctional Carbon Nanotubes for PH Sensing. *Mater. Lett.* **2016**, *176*, 68−70.

(2) Qin, Y.; Alam, A. U.; Howlader, M. M. R.; Hu, N. X.; Deen, M. J. Inkjet Printing of a Highly Loaded Palladium Ink for Integrated, Low-Cost PH Sensors. *Adv. Funct. Mater.* **2016**, *26*, 4923−4933.

(3) Martins, P.; Pereira, N.; Lima, A. C.; Garcia, A.; Mendes-Filipe, C.; Policia, R.; Correia, V.; Lanceros-Mendez, S. Advances in Printing

and Electronics: From Engagement to Commitment. *Advanced Functional Materials*; John Wiley and Sons Inc. April 18, 2023; Vol. 33.

(4) Tafoya, R. R.; Secor, E. B. Understanding and Mitigating Process Drift in Aerosol Jet Printing. *Flexible Printed Electron.* 2020, 5 (1), 015009.

(5) Fisher, C.; Skolrood, L. N.; Li, K.; Joshi, P. C.; Aytug, T. Aerosol-Jet Printed Sensors for Environmental, Safety, and Health Monitoring: A Review. *Advanced Materials Technologies*; John Wiley and Sons Inc, 2023; Vol. 8.

(6) Xie, W.; Zhang, X.; Leighton, C.; Frisbie, C. D. 2D Insulator-Metal Transition in Aerosol-Jet-Printed Electrolyte-Gated Indium Oxide Thin Film Transistors. *Adv. Electron. Mater.* 2017, 3 (3), 1600369.

(7) Tarabella, G.; Vurro, D.; Lai, S.; D'Angelo, P.; Ascari, L.; Iannotta, S. Aerosol Jet Printing of PEDOT:PSS for Large Area Flexible Electronics. *Flexible Printed Electron.* 2020, 5 (1), 014005.

(8) Shao, F.; Wan, Q. Recent Progress on Jet Printing of Oxide-Based Thin Film Transistors. *J. Phys. D: Appl. Phys.* 2019, 52, 143002 . Institute of Physics Publishing February 1.

(9) Li, J. M.; Hu, C. C.; Wu, T. H.; Hsu, Y. J. Electroless Deposition of RuO_2 -Based Nanoparticles for Energy Conversion Applications. *RSC Adv.* 2019, 9 (8), 4239−4245.

(10) Islam, M. R.; Afroj, S.; Novoselov, K. S.; Karim, N. Smart Electronic Textile-Based Wearable Supercapacitors. *Advanced Science*; John Wiley and Sons Inc., 2022; Vol. 9.

(11) Javed, M. S.; Najam, T.; Hussain, I.; Idrees, M.; Ahmad, A.; Imran, M.; Shah, S. S. A.; Luque, R.; Han, W. Fundamentals and Scientific Challenges in Structural Design of Cathode Materials for Zinc-Ion Hybrid Supercapacitors. *Advanced Energy Materials*; John Wiley and Sons Inc, 2023; Vol. 13.

(12) Atrak, N.; Tayyebi, E.; Skúlason, E. Insight into Catalytic Active Sites on TiO_2/RuO_2 and SnO_2/RuO_2 Alloys for Electrochemical CO_2 Reduction to CO and Formic Acid. *ACS Catal.* 2023, 13 (8), 5491−5501.

(13) Taheri, M.; Deen, M. J. Green Approach Using RuO_2/GO Nanocomposite for Low Cost and Highly Sensitive PH Sensing. *J. Electrochem. Soc.* 2022, 169 (4), 047501.

(14) Li, J. M.; Hu, C. C.; Wu, T. H.; Hsu, Y. J. Electroless Deposition of RuO_2 -Based Nanoparticles for Energy Conversion Applications. *RSC Adv.* 2019, 9 (8), 4239−4245.

(15) Gong, Y.; Liu, R.; Jiang, L.; Peng, A.; Xu, C.; Lu, X.; Ma, R.; Fu, Y.; Zhu, W.; Wang, S.; Zhou, L. Catalyst Development for HCl Oxidation to Cl_2 in the Fluorochemical Industry. *ACS Catal.* 2022, 12 (2), 1098−1110.

(16) Li, L.; Zhang, G.; Xu, J.; He, H.; Wang, B.; Yang, Z.; Yang, S. Optimizing the Electronic Structure of Ruthenium Oxide by Neodymium Doping for Enhanced Acidic Oxygen Evolution Catalysis. *Adv. Funct. Mater.* 2023, 33, 2213304.

(17) Atrak, N.; Tayyebi, E.; Skúlason, E. Electrochemical CO_2 Reduction towards Formic Acid and Methanol on Transition Metal Oxide Surfaces as a Function of CO Coverage. *Catal. Sci. Technol.* 2023, 13 (11), 3321−3336.

(18) Pu, J.; Shen, Z.; Zhong, C.; Zhou, Q.; Liu, J.; Zhu, J.; Zhang, H. Electrodeposition Technologies for Li-Based Batteries: New Frontiers of Energy Storage. *Advances in Materials*; Wiley-VCH Verlag, 2020; Vol. 32.

(19) Sarmah, B.; Satpati, B.; Srivastava, R. Selective Oxidation of Biomass-Derived Alcohols and Aromatic and Aliphatic Alcohols to Aldehydes with O_2/Air Using a RuO_2-Supported Mn_3O_4 Catalyst. *ACS Omega* 2018, 3 (7), 7944−7954.

(20) Zhang, S.; Wang, Y.; Qu, F.; Thomas, T.; Yang, M. In_2O_3 Nanocubes Modified with RuO_2 for Detection of TXM Vapors Containing Benzyl Group. *Sens. Actuators, B* 2021, 338, 129731.

(21) Uppuluri, K.; Lazouskaya, M.; Szwagierczak, D.; Zaraska, K.; Tamm, M. Fabrication, Potentiometric Characterization, and Application of Screen-Printed RuO_2 PH Electrodes for Water Quality Testing. *Sensors* 2021, 21 (16), 5399.

(22) Tseng, S. C.; Wu, T. Y.; Chou, J. C.; Liao, Y. H.; Lai, C. H.; Yan, S. J.; Tseng, T. W. Investigation of Sensitivities and Drift Effects of the Arrayed Flexible Chloride Sensor Based on RuO_2/GO at Different Temperatures. *Sensors* 2018, 18 (2), 632.

(23) Alam, M. M.; Mukhlish, M. Z. b.; Tazrin, A.; Jui, N. A.; Asiri, A. M.; Rahman, M. M.; Islam, M. A.; Uddin, M. T. A Novel Highly Selective Electrochemical Chlorobenzene Sensor Based on Ternary Oxide $RuO_2/ZnO/TiO_2$nanocomposites. *RSC Adv.* 2020, 10 (54), 32532−32547.

(24) Ravi, P. P.; Lindner, J.; Oechsner, H.; Lemmer, A. Effects of Target PH-Value on Organic Acids and Methane Production in Two-Stage Anaerobic Digestion of Vegetable Waste. *Bioresour. Technol.* 2018, 247, 96−102.

(25) Lian, Y.; Zhang, W.; Ding, L.; Zhang, X.; Zhang, Y.; Wang, X. d. Nanomaterials for Intracellular PH Sensing and Imaging. *Novel Nanomaterials for Biomedical, Environmental and Energy Applications*; Elsevier, 2019; pp 241−273.

(26) Manjakkal, L.; Szwagierczak, D.; Dahiya, R. Metal Oxides Based Electrochemical PH Sensors: Current Progress and Future Perspectives. *Prog. Mater. Sci.* 2020, 109 (December 2019), 100635.

(27) Alam, M. M.; Uddin, M. T.; Asiri, A. M.; Awual, M. R.; Fazal, M. A.; Rahman, M. M.; Islam, M. A. Fabrication of Selective L-Glutamic Acid Sensor in Electrochemical Technique from Wet-Chemically Prepared RuO_2 Doped ZnO Nanoparticles. *Mater. Chem. Phys.* 2020, 251, 123029.

(28) Hao, C.; Liao, Y.; Wu, Y.; An, Y.; Lin, J.; Gu, Z.; Jiang, M.; Hu, S.; Wang, X. RuO_2-Loaded TiO_2-MXene as a High Performance Photocatalyst for Nitrogen Fixation. *J. Phys. Chem. Solids* 2020, 136, 109141.

(29) Mingels, R. H. G.; Kalsi, S.; Cheong, Y.; Morgan, H. Iridium and Ruthenium Oxide Miniature PH Sensors: Long-Term Performance. *Sens. Actuators, B* 2019, 297, 126779.

(30) Lonsdale, W.; Shylendra, S. P.; Brouwer, S.; Wajrak, M.; Alameh, K. Application of Ruthenium Oxide PH Sensitive Electrode to Samples with High Redox Interference. *Sens. Actuators, B* 2018, 273, 1222−1225.

(31) Janczak, D.; Peplowski, A.; Wroblewski, G.; Gorski, L.; Zwierkowska, E.; Jakubowska, M. Investigations of Printed Flexible pH Sensing Materials Based on Graphene Platelets and Submicron RuO_2Powders. *J. Sens.* 2017, 2017 (Iv), 1−6.

(32) Das, S.; Mojumder, S.; Saha, D.; Pal, M. Influence of Major Parameters on the Sensing Mechanism of Semiconductor Metal Oxide Based Chemiresistive Gas Sensors: A Review Focused on Personalized Healthcare. *Sensor. Actuator. B Chem.* 2022, 352, 131066.

(33) Wu, Z. S.; Wang, D. W.; Ren, W.; Zhao, J.; Zhou, G.; Li, F.; Cheng, H. M. Anchoring Hydrous RuO_2 on Graphene Sheets for High-Performance Electrochemical Capacitors. *Adv. Funct. Mater.* 2010, 20 (20), 3595−3602.

(34) Park, S.; Lee, K. S.; Bozoklu, G.; Cai, W.; Nguyen, S. T.; Ruoff, R. S. Graphene Oxide Papers Modified by Divalent Ions - Enhancing Mechanical Properties via Chemical Cross-Linking. *ACS Nano* 2008, 2 (3), 572−578.

(35) Wilkinson, N. J.; Smith, M. A. A.; Kay, R. W.; Harris, R. A. A Review of Aerosol Jet Printing—a Non-Traditional Hybrid Process for Micro-Manufacturing. *Int. J. Adv. Manuf. Technol.* 2019, 105 (11), 4599−4619.

(36) Secor, E. B. Principles of Aerosol Jet Printing. *Flexible Printed Electron.* 2018, 3 (3), 035002.

(37) Jadhav, S. v.; Nikam, D. S.; Khot, V. M.; Thorat, N. D.; Phadatare, M. R.; Ningthoujam, R. S.; Salunkhe, A. B.; Pawar, S. H. Studies on Colloidal Stability of PVP-Coated LSMO Nanoparticles for Magnetic Fluid Hyperthermia. *New J. Chem.* 2013, 37 (10), 3121−3130.

(38) Lu, G.; Li, S.; Guo, Z.; Farha, O. K.; Hauser, B. G.; Qi, X.; Wang, Y.; Wang, X.; Han, S.; Liu, X.; Duchene, J. S.; Zhang, H.; Zhang, Q.; Chen, X.; Ma, J.; Loo, S. C. J.; Wei, W. D.; Yang, Y.; Hupp, J. T.; Huo, F. Imparting Functionality to a Metal-Organic Framework Material by Controlled Nanoparticle Encapsulation. *Nat. Chem.* 2012, 4 (4), 310−316.

(39) Koczkur, K. M.; Mourdikoudis, S.; Polavarapu, L.; Skrabalak, S. E. Polyvinylpyrrolidone (PVP) in Nanoparticle Synthesis. *Dalton Trans.* **2015**, *44* (41), 17883–17905.

(40) Ziaei-Azad, H.; Semagina, N. Bimetallic Catalysts: Requirements for Stabilizing PVP Removal Depend on the Surface Composition. *Appl. Catal., A* **2014**, *482*, 327–335.

(41) Graf, C.; Dembski, S.; Hofmann, A.; Rühl, E. A General Method for the Controlled Embedding of Nanoparticles in Silica Colloids. *Langmuir* **2006**, *22* (13), 5604–5610.

(42) Ghorbani, M.; Abdizadeh, H.; Taheri, M.; Golobostanfard, M. R. Enhanced Photoelectrochemical Water Splitting in Hierarchical Porous ZnO/Reduced Graphene Oxide Nanocomposite Synthesized by Sol-Gel Method. *Int. J. Hydrogen Energy* **2018**, *43* (16), 7754–7763.

(43) Dresselhaus, M. S.; Jorio, A.; Hofmann, M.; Dresselhaus, G.; Saito, R. Perspectives on Carbon Nanotubes and Graphene Raman Spectroscopy. *Nano Lett.* **2010**, *10*, 751–758. March 10

(44) Mousli, F.; Chaouchi, A.; Jouini, M.; Maurel, F.; Kadri, A.; Chehimi, M. M. Polyaniline-Grafted RuO2-TiO2 Heterostructure for the Catalysed Degradation of Methyl Orange in Darkness. *Catalysts* **2019**, *9* (7), 578.

(45) He, H.; Dyck, M. F.; Horton, R.; Li, M.; Jin, H.; Si, B. *Distributed Temperature Sensing for Soil Physical Measurements and Its Similarity to Heat Pulse Method*, 1st; Elsevier Inc., 2018; Vol. 148.

(46) Lazouskaya, M.; Erlewein, S.; Yzombard, P.; Zimmermann, M.; Kellerbauer, A. Nafion Protective Membrane Enables Using Ruthenium Oxide Electrodes for PH Measurement in Milk. *J. Electrochem. Soc.* **2021**, *168*, 107511.

(47) Johnson, J. R. T.; Panas, I. Water Adsorption and Hydrolysis on Molecular Transition Metal Oxides and Oxyhydroxides. *Inorg. Chem.* **2000**, *39* (15), 3181–3191.

(48) Brown, G. E.; Henrich, V. E.; Casey, W. H.; Clark, D. L.; Eggleston, C.; Felmy, A.; Goodman, D. W.; Grätzel, M.; Maciel, G.; McCarthy, M. I.; Nealson, K. H.; Sverjensky, D. A.; Toney, M. F.; Zachara, J. M. Metal Oxide Surfaces and Their Interactions with Aqueous Solutions and Microbial Organisms. *Chem. Rev.* **1999**, *99* (1), 77–174.

(49) Kurzweil, P. Metal Oxides and Ion-Exchanging Surfaces as PH Sensors in Liquids: State-of-the-Art and Outlook. *Sensors* **2009**, *9* (6), 4955–4985.

(50) Sardarinejad, A.; Maurya, D. K.; Khaled, M.; Alameh, K. Temperature Effects on the Performance of RuO2 Thin-Film PH Sensor. *Sens. Actuators, A* **2015**, *233*, 414–421.

(51) Xu, B.; Zhang, W. Modification of vertically aligned carbon nanotubes with RuO2 for a solid-state pH sensor. *Electrochim. Acta* **2010**, *55* (8), 2859–2864.

(52) Chawang, K.; Bing, S.; Chiao, J. C. Printable and Flexible Iridium Oxide-Based PH Sensor by a Roll-to-Roll Process. *Chemosensors* **2023**, *11* (5), 267.

(53) Alam, A. U.; Clyne, D.; Deen, M. J. A Low-Cost Multi-Parameter Water Quality Monitoring System. *Sensors* **2021**, *21* (11), 3775.

(54) Alam, A. U.; Clyne, D.; Jin, H.; Hu, N. X.; Deen, M. J. Fully Integrated, Simple, and Low-Cost Electrochemical Sensor Array for in Situ Water Quality Monitoring. *ACS Sens.* **2020**, *5* (2), 412–422.

(55) Lonsdale, W.; Shylendra, S. P.; Wajrak, M.; Alameh, K. Application of All Solid-State 3D Printed PH Sensor to Beverage Samples Using Matrix Matched Standard. *Talanta* **2019**, *196*, 18–21.

(56) Mingels, R. H. G.; Kalsi, S.; Cheong, Y.; Morgan, H. Iridium and Ruthenium Oxide Miniature PH Sensors: Long-Term Performance. *Sens. Actuators, B* **2019**, *297*, 126779.

(57) Zea, M.; Moya, A.; Fritsch, M.; Ramon, E.; Villa, R.; Gabriel, G. Enhanced Performance Stability of Iridium Oxide-Based PH Sensors Fabricated on Rough Inkjet-Printed Platinum. *ACS Appl. Mater. Interfaces* **2019**, *11* (16), 15160–15169.

(58) Tanumihardja, E.; Olthuis, W.; van den Berg, A. Ruthenium Oxide Nanorods as Potentiometric Ph Sensor for Organs-on-Chip Purposes. *Sensors* **2018**, *18* (9), 2901.

(59) Lonsdale, W.; Maurya, D. K.; Wajrak, M.; Alameh, K. Effect of Ordered Mesoporous Carbon Contact Layer on the Sensing Performance of Sputtered RuO2 Thin Film PH Sensor. *Talanta* **2017**, *164*, 52–56.